Scattering-free modulation of elastic shear-horizontal waves based on interface impedance theory

Mu Jiang, Yan-Feng Wang, Badreddine Assouar, Yue-Sheng Wang

▶ **To cite this version:**

Mu Jiang, Yan-Feng Wang, Badreddine Assouar, Yue-Sheng Wang. Scattering-free modulation of elastic shear-horizontal waves based on interface impedance theory. Physical Review Applied, 2024, 20 (5), pp.054020. 10.1103/PhysRevApplied.20.054020 . hal-04276616

HAL Id: hal-04276616
https://hal.science/hal-04276616v1

Submitted on 9 Nov 2023

HAL is a multi-disciplinary open access archive for the deposit and dissemination of scientific research documents, whether they are published or not. The documents may come from teaching and research institutions in France or abroad, or from public or private research centers.

L'archive ouverte pluridisciplinaire **HAL**, est destinée au dépôt et à la diffusion de documents scientifiques de niveau recherche, publiés ou non, émanant des établissements d'enseignement et de recherche français ou étrangers, des laboratoires publics ou privés.

Scattering-free modulation of elastic shear-horizontal waves based on interface impedance theory

Mu Jiang,[1,2] Yan-Feng Wang*,[1] Badreddine Assouar†,[2] and Yue-Sheng Wang‡[1,3]

[1]*School of Mechanical Engineering, Tianjin University, 300350 Tianjin, China*

[2]*Institut Jean Lamour, CNRS, Universite de Lorraine, Nancy, 54000, France*

[3]*Institute of Engineering Mechanics,*

Beijing Jiaotong University, 100044 Beijing, China

Abstract

Elastic metasurfaces are mostly conceived and designed based on gradient phase and thus suffering from parasitic scattering. Inspired by the advances of surface impedance model in acoustics, in this research, we establish an interface impedance model to realize scattering-free modulation of elastic shear-horizontal (SH) waves. Anomalous refraction at large angle is successfully obtained through interface impedance. Meanwhile, focusing and Airy beam generation are also investigated, which are mostly achieved by phase-based structures. We provide lossless or lossy forms of impedance to suppress parasitic waves. The establishment of boundaries with different shapes has been discussed. Finally, the simulated results of elastic metasurfaces composed of optimized units further validates the feasibility of impedance theory in achieving precise manipulation of SH waves.

Keywords: Interface impedance, SH wave, elastic Metasurface, Focusing, Airy beam

* Corresponding authors.E-mail: wangyanfeng@tju.edu.cn

† Corresponding authors.E-mail: badreddine.assouar@univ-lorraine.fr

‡ Corresponding authors.E-mail: yswang@tju.edu.cn

1. INTRODUCTION

Metasurfaces with gradient phase[1] allows the modulation of wavefronts by compact and simply fabricated structures. Their emergence also bring additional freedom of research both academically and practically. Inspired by the developments of electromagnetism[1, 2] and acoustics[3–5], elastic metasurafces further arise the interests of researchers. For the rich modes of elastic waves[6–8] and wide applications, such as vibration control[9], non-destructive testing[10], imaging[11], etc., there is broad space and immense value for the related study on elastic metasurfaces.

Currently, most of elastic metasurfaces are designed according to the generalized Snell's law (GSL). The composed units are supposed to fulfill the desired phase distribution for the corresponding functionality, such as anomalous refraction[12, 13]/reflection[9, 14], focusing[15, 16], self-bending beam[12, 17–20] and illusion[12, 21–23]. Some units are resonant type, including plate-based pillars[14, 24–26] and embedded microstructures[9, 13, 27–29]. Others resemble beams and are designed by stacking materials[30–32] or extending propagation path of elastic waves[33–38]. However, the phase gradient metasurfaces only designate the desired order of waves[39]. The unspecified waves in higher orders can propagate in scattered directions and affect the overall performance, which is unignorable with the increasing requirement of precise manipulation.

Thereupon, metagratings are continuously designed to eliminate the scattered waves according to diffraction theory[40]. Since the unwanted high-order scattering modes can be theoretically identified and suppressed, functionalities are developed for more precise manipulation. Wave trapping[41] and retroreflection[42] can be attained by selecting the desired order of diffraction. Through the enhancement and suppression of different orders of diffracted waves, wave splitting[39] with the desired amplitudes and enhanced absorption[43] have been successfully realized. It is also possible to achieve asymmetric transmission[44] by utilizing the integer-parity feature of metasurfaces. Additionally, by defining the objective function with diffraction orders[45], the unwanted modes can be suppressed directly by optimization. However, the above mentioned methods are only applied for periodic structures.

Recently, surface impedance model[46] was proposed in acoustics to fully avoid the generation of parasitic scattering. With the introduction of bianisotropic units[47], the theoretical requirement of impedance can be fulfilled by structures and precise acoustic transmission is

achievable practicably. As the impedance theory expands, no matter the functionalities rely on periodic structures(refraction[47], splitting[48] and generation of angular momentum[49]) or not(focusing[50]), their performances can all be demonstrated more accurately. In spite of the extensive research on acoustic metasurfaces based on impedance theory, the work about elastic metasurfaces are rarely reported. Progress has been made recently that an impedance-based elastic metasurface[51] can achieve efficient reflection of flexural waves. However, there is still ample room for further exploration of transmissive elastic metasurface based on interface impedance theory.

In this work, we present transmissive metasurfaces based on interface impedance theory to realize precise manipulation of elastic SH waves. Firstly, we establish an interface impedance model for calculating SH waves, which can present an accurate wave field. Secondly, we derive the expression of impedance matrix for achieving precise refraction, focusing and Airy beam generation using lossless or lossy forms. The theoretical wave fields without parasitic scattering can be obtained successfully. Curved interfaces are also considered, providing the possibility of designing metasurfaces in multiple shapes. Finally, elastic metasurfaces are constructed by lossless units optimized according to impedance requirements. The simulated results of metasurfaces verify the correctness and effectiveness of the interface impedance model.

2. INTERFACE IMPEDANCE MODEL FOR ELASTIC SH WAVES

Fig. 1 depicts the schematic diagram of an interface impedance model for precise manipulation of SH waves. The impedance-described interface is determined by the extraodinary functionalities exhibited in the transmitted field, including refraction, focusing and Airy beam generation. By employing the appropriate impedance, the desired fields can be realized without parasitic waves. The design of elastic metasurfaces is guided by the impedance requirements and can then be accomplished through an optimization algorithm. It is worthy to note that an interface impedance boundary condition is deduced and applied in the finite element model (FEM) in COMSOL Multiphysics software to perform accurate wave fields in this work. The details can be found in supplementary material.

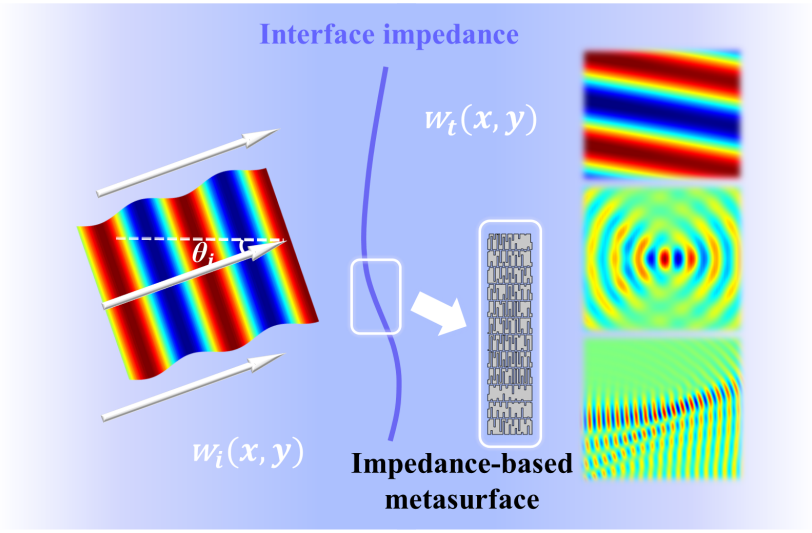

FIG. 1: Illustration of the desired wave fields formed through the interface impedance model. The corresponding elastic metasurfaces can be designed according to the theoretically required impedance.

2.1. Anomalous refraction

We first consider the precise realization of anomalous refraction according to the interface impedance theory. Considering the wave equation of SH wave $\nabla[G\nabla w] = -\rho\omega^2 w$, the displacement field of incident waves can be obtained, as well as the corresponding stress vector and velocity. Here, ω is the angular frequency, the medium is chosen as steel with Young's modulus $E = 194.02$ GPa, Poisson's ratio $\nu = 0.3$ and density $\rho = 7930\text{kg/m}^2$. The shear modulus can be calculated as $G = \frac{E}{2(1+\nu)}$. Given the mechanical intensity vector[52] as $\vec{I} = \frac{1}{2}Re(\sigma_{ij} \cdot v_j{}^*)$ $(i, j = x, y, z)$, its normal component can then be derived with the normal unit vector $\hat{n} = n_x \cdot \hat{x} + n_y \cdot \hat{y}$. The expressions of the above fields can be described as follows:

$$w_i = Ae^{-ik\sin\theta_i x}e^{ik\cos\theta_i y} \tag{1a}$$

$$\vec{\sigma_i} = -i\omega Z_0 w_i(\sin\theta_i\hat{x} - \cos\theta_i\hat{y}) \tag{1b}$$

$$v_i = -i\omega w_i \tag{1c}$$

$$I_i = \frac{1}{2}Z_0\omega^2 A^2(\sin\theta_i n_x - \cos\theta_i n_y) \tag{1d}$$

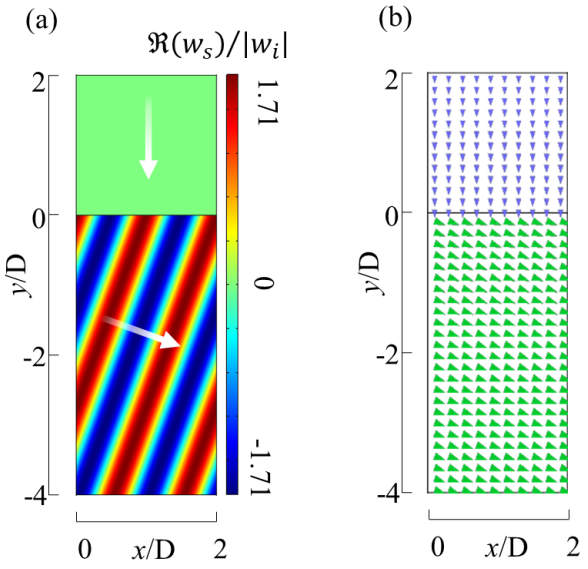

FIG. 2: (a)The wave field of anomalous refraction at $\theta_t = 70°$ realized through the lossless form of impedance. (b)The intensity vector distribution is presented by the arrows with scale factor 0.5.

where A is the amplitude of the incident wave at angle θ_i. The wave number is $k = \omega/c$ and the characteristic impedance is $Z_0 = \rho c$, where c denotes the wave velocity $c = \sqrt{\frac{G}{\rho}}$. The part $N_i = \sin\theta_i n_x - \cos\theta_i n_y$ is written for simplicity.

The transmitted wave field is set and other fields can then be obtained as

$$\begin{aligned} w_{t1} &= B_1 e^{-ik\sin\theta_t x} e^{ik\cos\theta_t y} \\ \vec{\sigma_{t1}} &= -i\omega Z_0 w_{t1}(\sin\theta_t \hat{x} - \cos\theta_t \hat{y}) \\ v_{t1} &= -i\omega w_{t1} \\ I_{t1} &= \frac{1}{2} Z_0 \omega^2 {B_1}^2 (\sin\theta_t n_x - \cos\theta_i n_y) \end{aligned} \tag{2}$$

where B_1 is the amplitude of the refracted wave at angle θ_t. The mechanical impedance is defined as the ratio between the excitation force and the velocity response[53]. We define it as $Z = \hat{n} \cdot \vec{\sigma}/v$ to simplify the analysis. Then the interface impedance between incident and transmitted field can be described as

$$\begin{bmatrix} -\hat{n}\cdot\vec{\sigma}_i \\ \hat{n}\cdot\vec{\sigma}_t \end{bmatrix} = \begin{bmatrix} Z_{11} & Z_{12} \\ Z_{21} & Z_{22} \end{bmatrix} \begin{bmatrix} v_i \\ v_t \end{bmatrix} = \begin{bmatrix} iX_{11} & iX_{12} \\ iX_{21} & iX_{22} \end{bmatrix} \begin{bmatrix} v_i \\ v_t \end{bmatrix} \tag{3}$$

The constraint on the normal energy intensity is set as $I_i = I_t$ to reach unitary efficiency

and the ratio of amplitudes can be solved as $tr_1 = B_1/A = \sqrt{\cos\theta_i/\cos\theta_t}$. Finally, the components of impedance matrix can be expressed as

$$\begin{aligned} X_{11} &= Z_0 \cot\Phi \cos\theta_i \\ X_{12} &= X_{21} = -Z_0 \frac{\cos\theta_i}{tr_1 \sin\Phi} \\ X_{22} &= Z_0 \cot\Phi \cos\theta_t \end{aligned} \tag{4}$$

where $\varphi_i = k(\sin\theta_i x - \cos\theta_i y)$, $\varphi_t = k(\sin\theta_t x - \cos\theta_t y)$ and $\Phi = \varphi_i - \varphi_t$. The components are plotted in Fig. 8(a).

The simulated result of refraction at 70° over two periods is given in Fig. 2(a). Here, the period is $D = \lambda/|\sin\theta_t - \sin\theta_i|$ and the wavelength is $\lambda = 0.3068$m under the target frequency 10kHz. At this point, the energy distribution is uniform and power flow-conservation condition is satisfied. The lossless impedance solution allows the incident wave to pass through the boundary smoothly without any scattering waves, which can be observed from the intensity vector distribution plotted in Fig. 2(b).

2.2. Focusing

We consider the process of focusing as a conversion from a plane wave to a cylindrical wave. Thus, the displacement field of focusing can be represented by the first-order Hankel function of the first kind $H_1^1(kr)$ with amplitude B_2 as

$$\begin{aligned} w_{t2} &= B_2 H_1^1(kr) \\ \vec{\sigma_{t2}} &= \frac{1}{2}\omega Z_0 B_2 [H_0^1(kr) - H_2^1(kr)](\frac{x - x_f}{r}\hat{x} + \frac{y - y_f}{r}\hat{y}) \\ v_{t2} &= -i\omega B_2 H_1^1(kr) \\ I_{t2} &= \frac{1}{4} Z_0 \omega^2 {B_2}^2 \gamma N_f \end{aligned} \tag{5}$$

where $r = \sqrt{(x - x_f)^2 + (y - y_f)^2}$ is the polar radius, (x_f, y_f) is the focusing point set as (0,-2.282λ). The Hankel function can also be expressed by the Bessel function of the first kind as $H_1^1(kr) = J_1^1(kr) + iY_1^1(kr)$. Given the simplified forms $\gamma = Y_1^1(kr)[J_0^1(kr) - J_2^1(kr)] - J_1^1(kr)[Y_0^1(kr) - Y_2^1(kr)]$ and $N_f = \frac{x-x_f}{r} n_x + \frac{y-y_f}{r} n_y$, the ratio of amplitudes can

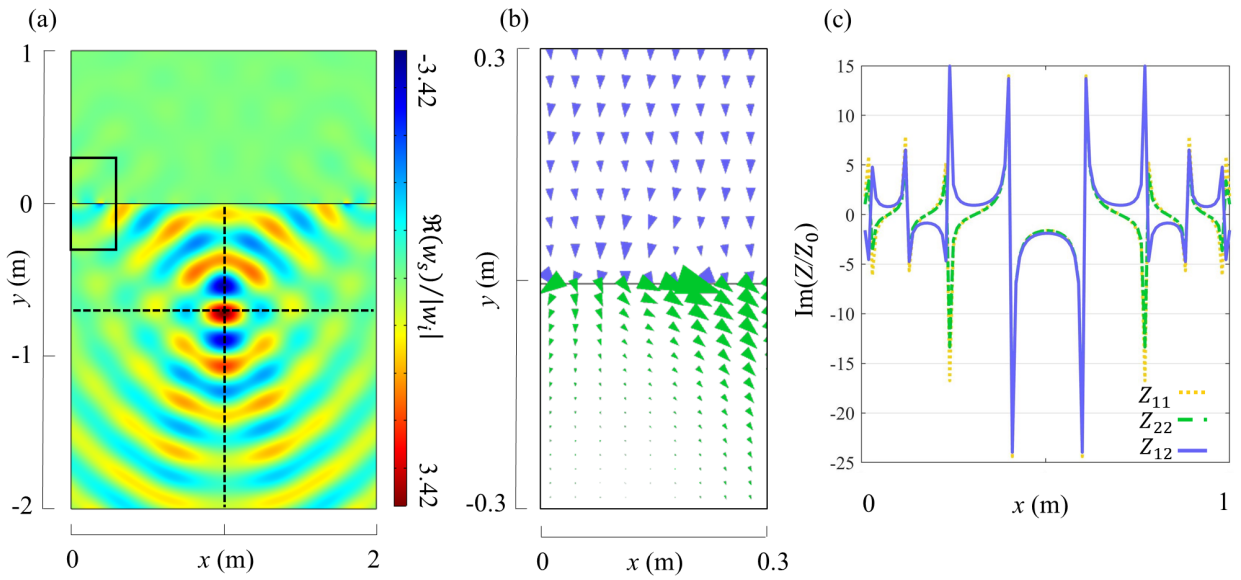

FIG. 3: (a)The focusing wave field realized through the lossless form of impedance. (b)The intensity vector distribution from the box-selected area in (a) is presented by the arrows with scale factor 0.5. (c)Curves of the impedance matrix with purely imaginary components are plotted.

be solved as $tr_2 = B_2/A = \sqrt{\frac{2N_i}{\gamma N_f}}$. The matrix elements in Eq. (3) for focusing can then be expressed as

$$
\begin{aligned}
X_{11} &= Z_0 N_i \frac{Y_1^1(kr)\sin\varphi_i - J_1^1(kr)\cos\varphi_i}{Y_1^1(kr)\cos\varphi_i + J_1^1(kr)\sin\varphi_i} \\
X_{12} &= X_{21} = \frac{Z_0 N_i}{tr_2} \frac{1}{Y_1^1(kr)\cos\varphi_i + J_1^1(kr)\sin\varphi_i} \\
X_{22} &= \frac{Z_0 N_f}{2} \frac{[J_0^1(kr) - J_2^1(kr)]\sin\varphi_i + [Y_0^1(kr) - Y_2^1(kr)]\cos\varphi_i}{Y_1^1(kr)\cos\varphi_i + J_1^1(kr)\sin\varphi_i}
\end{aligned}
\tag{6}
$$

Fig. 3(a) shows the focusing wave field forming through the impedance boundary defined above and the focal point is at (0,-2.282λ). It can be known that even if the focusing field is strictly implemented according to the impedance requirement, the location of focus point would differ from the theoretical value to some extent. The components of impedance matrix are depicted in Fig. 3(c). In this case, the normal component of the transmitted energy I_t varies on the boundary if the ratio of amplitudes is still a constant as the one for anomalous refraction. Thus, tr_2 is actually adjusting with the coordinate x. And the rapidly changing amplitude causes small fluctuations near the boundary at the same time. To observe this

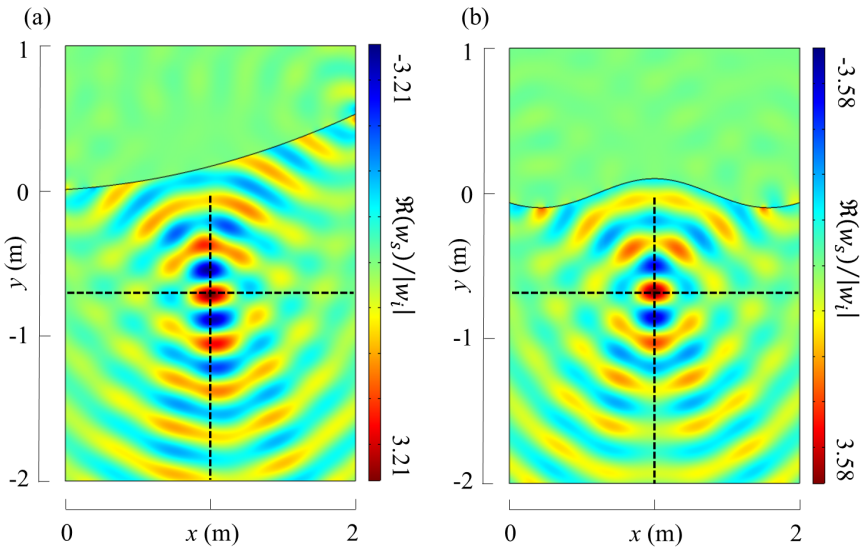

FIG. 4: The focusing wave field for (a)parabolic boundary and (b)sinusoidal boundary realized through the lossless form of impedance.

process clearly, the energy intensity vectors in the box-selected area from Fig. 3(a) are plotted in Fig. 3(b).

The curve-shaped boundaries are also considered and the unit normal vector $\hat{n}$ is changed accordingly. Here, the shape of the boundary is applied as parabolic curve $y = a_0x^2$ in Fig. 4(a) and sine curve $y = a_0 \cos \omega_0 x$ in Fig. 4(b). The unit normal vector is then adjusted as $(-2a_0x/\sqrt{4a_0{}^2x^2+1}, 1/\sqrt{4a_0{}^2x^2+1})$ and $(\omega_0 a_0 \sin \omega_0 x/\sqrt{-\omega_0 a_0 \sin \omega_0 x^2+1}, 1/\sqrt{-\omega_0 a_0 \sin \omega_0 x^2+1})$ respectively. The focal points in the simulations locate at (-0.013λ,-2.135λ) for parabolic boundary and (0,-2.155λ) for sinusoidal boundary. The slight deviation of the focus position comes from the asymmetric shape of the boundaries.

2.3. Airy beam generation

For refraction and focusing, the power flow-conservation condition can be fulfilled by designating amplitudes on the boundary, because the normal components of energy intensity in the incident and transmitted fields point at the same direction. However, these components can point at different directions for Airy beam, indicating that energy shouldn't passing through the boundary at specific positions. These impermissible energies can be tackled by being redirected elsewhere[54] or being absorbed on site. Here, the energy is processed by

the second way, which determines the existence of real components in impedance matrix, as Eq. (7) denotes.

$$\begin{bmatrix} -\hat{n}\cdot\vec{\sigma_i} \\ \hat{n}\cdot\vec{\sigma_t} \end{bmatrix} = \begin{bmatrix} Z_{11} & Z_{12} \\ Z_{21} & Z_{22} \end{bmatrix} \begin{bmatrix} v_i \\ v_t \end{bmatrix} = \begin{bmatrix} iX_{11} & R+iX_{12} \\ R+iX_{21} & iX_{22} \end{bmatrix} \begin{bmatrix} v_i \\ v_t \end{bmatrix} \tag{7}$$

Next, with the expression of the desired wavefield provided, further calculations can be performed. The wave field of Airy beam can be represents by the Airy function $Ai(s-\frac{\xi^2}{4})$, where $s=x/x_0$ represents the transverse scale normalized by the Airy characteristic length, $\xi = y/k{x_0}^2$ denotes the normalized propagation distance. And different fields for Airy beam generation can be expressed as

$$\begin{aligned} w_{t3} &= B_3 Ai(g)e^{ig} \\ \vec{\sigma_{t3}} &= B_3 G e^{ig}\{\frac{1}{x_0}[\frac{\partial Ai(g)}{\partial x}+Ai(g)\frac{i\xi}{2}]\hat{x}+\frac{1}{k{x_0}^2}[-\frac{\xi}{2}\frac{\partial Ai(g)}{\partial y}+i(\frac{s}{2}-\frac{\xi^2}{4})Ai(g)]\hat{y}\} \\ v_{t3} &= -i\omega B_3 Ai(g)e^{ig} \\ I_{t3} &= -\frac{1}{2}G\omega {B_3}^2 Ai(g)^2 N_a \end{aligned} \tag{8}$$

where we have concise forms as $g(s,\xi)=\frac{s\xi}{2}-\frac{\xi^3}{12}$, $N_a=\frac{1}{x_0}\frac{\xi}{2}n_x+\frac{1}{k{x_0}^2}(\frac{s}{2}-\frac{\xi^2}{4})n_y$. The relationship $Z_{12}=Z_{21}$ still remains and the expressions of matrix components can be given as

$$\begin{aligned} X_{11} &= Z_0\frac{-4N_i k^2{x_0}^2\cos^2 2\phi+{tr_3}^2 Ai(g)^2[n_y(2s-\xi^2)+n_x 2kx_0\xi]}{4k^2{x_0}^2\sin 2\phi Ai(g)} \\ X_{12} &= X_{21} = Z_0\frac{4N_i k^2{x_0}^2-{tr_3}^2 Ai(g)^2[n_y(2s+\xi^2)-n_x 2kx_0\xi]}{8tr_3 k^2{x_0}^2\sin\phi Ai(g)} \\ R &= -Z_0\frac{4N_i k^2{x_0}^2+{tr_3}^2 Ai(g)^2[n_y(2s-\xi^2)+n_x 2kx_0\xi]}{8tr_3 k^2{x_0}^2\cos\phi Ai(g)} \\ X_{22} &= -Z_0\frac{4N_i k^2 x_0^2+{tr_3}^2 Ai(g)^2\cos\phi[n_y(2s-\xi^2)+n_x 2kx_0\xi]}{4k^2{x_0}^2\sin 2\phi Ai(g)^2}+Z_0\frac{{tr_3}^2[\frac{\partial Ai(g)}{\partial y}n_y\xi-\frac{\partial Ai(g)}{\partial x}n_x 2kx_0]}{2k^2{x_0}^2 Ai(g)} \end{aligned} \tag{9}$$

where $\phi=g(s,\xi)+\varphi_i$, $x_0=0.4$.

Setting the boundary shape as a straight line will make the denominators of the impedance matrix components be zero. Thus, we set the boundary into arc shape and its unit normal

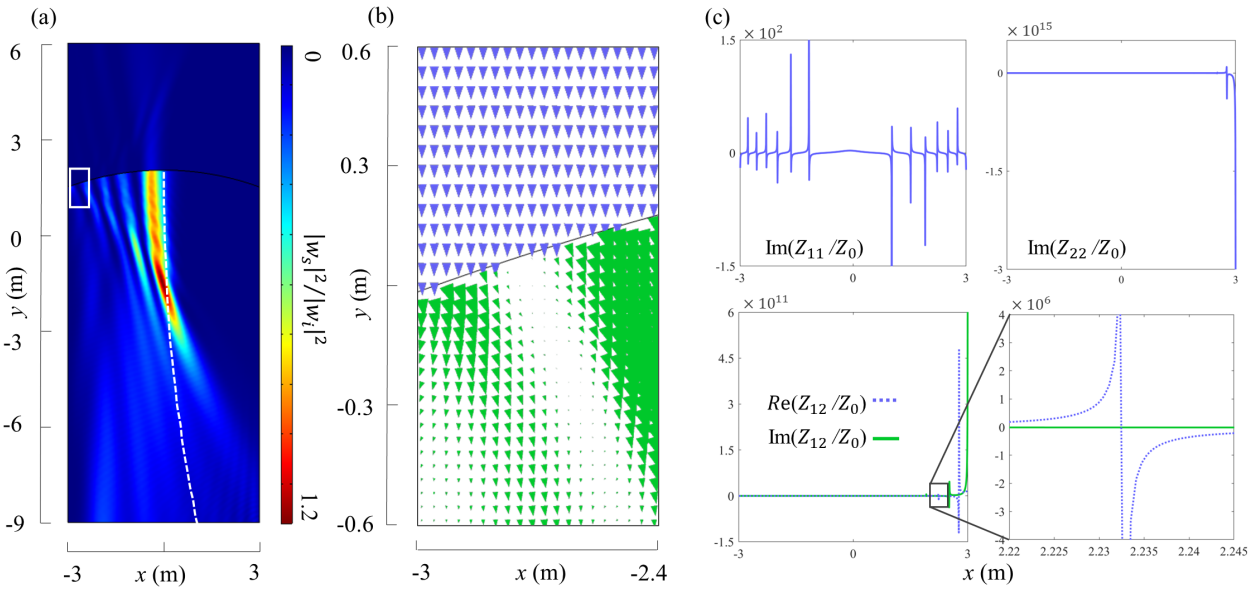

FIG. 5: (a)The normalized intensity field for arc-shaped boundary realized through the lossy form of impedance. The theoretical trajectory is marked by dashed lines. (b)The intensity vector distribution near the boundary is presented by the arrows with scale factor 1 for incident field and 10 for transmitted field. (c)Curves of the impedance matrix with both real and imaginary components along the arc boundary are plotted.

vector is $(\frac{x-x_0}{R_0}, \frac{y-y_0}{R_0})$, where (x_0, y_0) is the center of the arc and R_0 is the radius. Though there exist loss and gain inside the interface, corresponding to positive and negative R, the system can be lossless by equating the overall power between the incident and transmitted sides[50, 55]. The detailed process of calculating amplitudes ratio is provided in the supplementary material. In this way, the ratio of amplitudes can be solved as $tr_3 = B_3/A = 1.3356$. The normalized intensity field is shown in Fig. 5(a). It can be observed that the main lobe falls on the theoretical trajectory. The energy distribution in the box-selected area is shown in Fig. 5(b) for a clear observation. Portion of energy is absorbed after passing through a section of boundary with loss, resulting in a low output of energy in the transmitted field. This progress can be perceived from the change in size of the arrows. The curves of impedance matrix are shown in Fig. 5(c), as long as a zoom-in plot of the area with the first spike of R. Except from this spike, R remains positive in the regions along $-x$ direction. It only exhibits oscillations and negative values(gain) near $x = 3m$.

Similarly, Airy beam can be generated through boundaries in various shapes, and the simulations for parabolic and cosine boundaries are presented in Fig. 6. Considering the balanced power between incident and transmitted sides, the amplitudes ratio can obtained

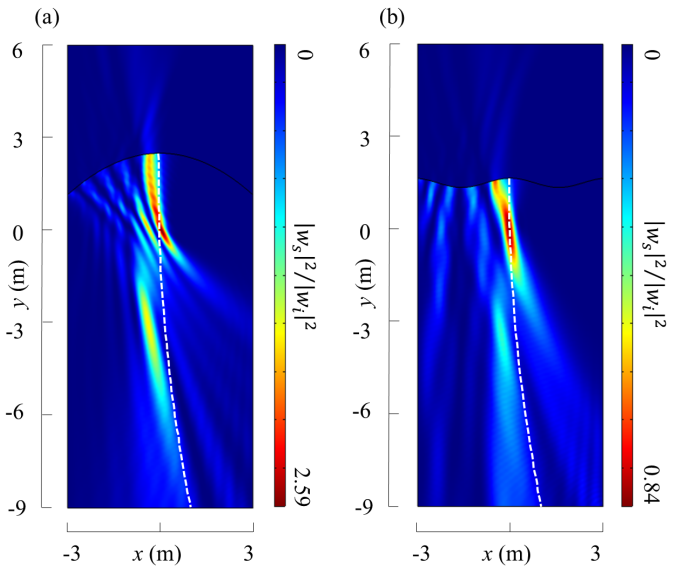

FIG. 6: The normalized intensity field of Airy beam for (a)parabolic boundary and (b)cosine boundary realized through the lossy form of impedance. The theoretical trajectory is marked by dashed lines.

correspondingly as 1.6485 and 1.2592. The main lobes all fall on the theoretical trajectories. In Fig. 6(a), the main lobe of the Airy beam is formed as a more curved profile with higher intensity than the ones in Fig. 5(a) and Fig. 6(b). This can be resulted from the continuous positive slope on the left side of the parabolic curve, making the side lobes converge to the center. On the contrary, side lobes in Fig. 6(b) can be observed to scatter away from the center.

3. METASURFACE DESIGN

The aforementioned simulations presented the validity of achieving functionalities through a single impedance boundary without parasitic scattering. To give a further proof of the theoretical concepts, a metasurface implemented by lossless units is designed. Here, the genetic algorithm is applied to optimize the units meeting the impedance requirements.

Considering that zigzag structure does not rely on resonant mechanism primarily, the losses caused by unit resonance can be avoided as much as possible. Fig. 7 illustrates the functional unit that is to be optimized, which is based on zigzag structure. The width H_0 of a unit is D/N (N=12) for anomalous refraction and $6.52\lambda/N$ (N=32) for focusing. Slits with width $H_g = H_0/25$ on both sides of the unit are to avoid coupling. The thickness of

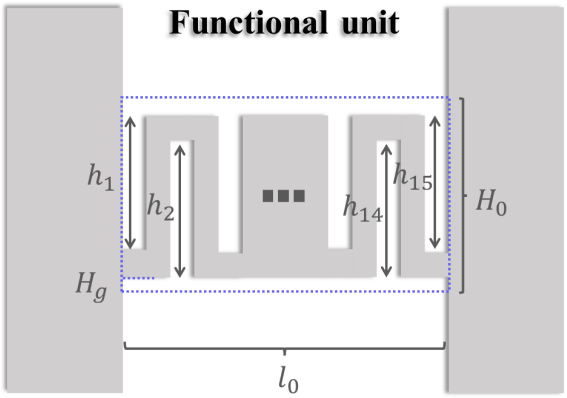

FIG. 7: The functional unit with zigzag structure is to be optimized.

the metasurface is $l_0 = 2.4H_0$, approximately $\lambda/4.7$ for refraction and $\lambda/2.1$ for focusing, fulfilling the subwavelength scale. 15 strips with length h_i(i=1,2,...,15) and width $l_0/29$ are removed to form the zigzag structure.

Here, parameters h_i are optimized by genetic algorithm to obtain units with required impedance. The optimization can be regardeded as obtaining the minimum of objective function F described as

$$\begin{aligned} F &= \frac{1}{3}\left(f_1 + f_2 + f_3\right) = \frac{1}{3}\sum_{(i,j)}\left|\frac{Z^o_{(i,j)} - Z^t_{(i,j)}}{Z^t_{(i,j)}}\right|, (i,j) = (1,1),(1,2),(2,2) \\ q_1 &= 0.2, F < 0.5 \text{ and } \max(f) - \min(f) > 0.7 \\ q_2 &= \max(f), \text{ if all the } f < 0.3 \end{aligned} \tag{10}$$

where the superscripts "o" and "t" represent the obtained and target values of impedance. The penalty term q mainly prevents excessive differences between matrix components during the early stage of optimization. It also helps to preferentially suppress the component that deviates the most from desired value when the matrix approaches the target.

To simply illustrate the correctness of the proposed method and the derived impedance solutions, lossless units are optimized and constructed into metasurfaces for refraction and focusing. The optimized parameters are all provided in supplementary material.

According to the impedance requirements of refraction formed by flat metasurface, the theoretical and optimized results are plotted in Fig. 8(a). The elastic metasurface can then be constructed and the wave field is realized as presented in Fig. 8(b). To evaluate the quality of refraction, the normalized amplitudes in different directions is performed and

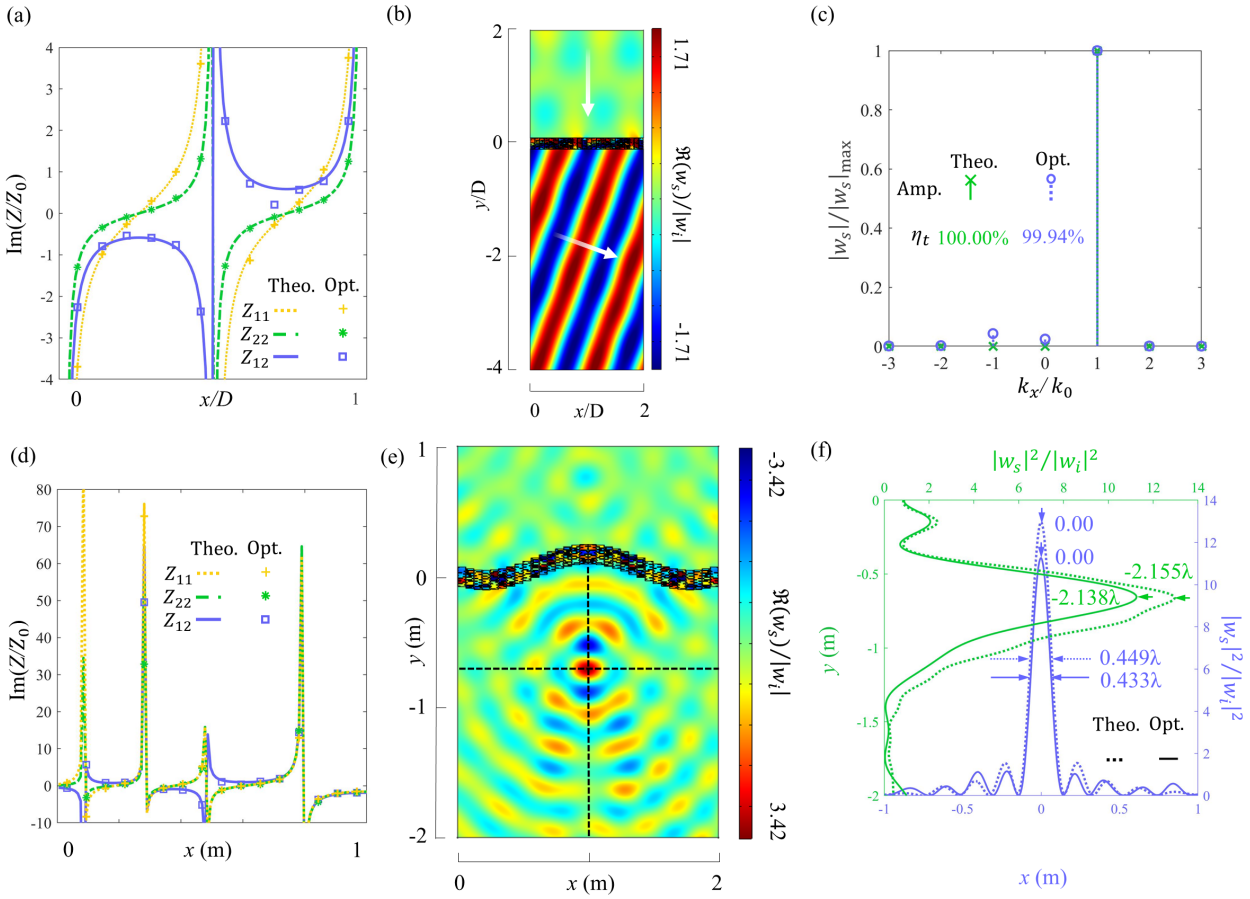

FIG. 8: The comparison of impedance between theoretical and optimized results for (a)refraction and (d)focusing. The displacement field realized by elastic metasurfaces composed of optimized units for (b)refraction and (e)focusing. (c)The normalized amplitudes at different refraction orders. (f)The intensities at the focal point.

illustrated in Fig. 8(c) by fast Fourier transformation. The refraction efficiency of the first-order transmitted mode is calculated by $\eta_t = \frac{|B_{1,-1}|^2}{\sum_{i=-1,0,1}|B_{1,-i}|^2}$, showing 99.94% for the optimized result and is obviously higher than the limitation of conventional designs.

As for focusing, the theoretical and optimized results of impedance are presented in Fig. 8(d). The corresponding elastic metasurface in cosine shape realizes the desired wave field successfully, as shown in Fig. 8(e). Slightly different from the theoretical one, the focal point locates at (0,-2.138λ). The deviation is mainly caused by the units being placed at positions with divergent impedance, which also results in the not fully suppressed -1 order diffraction in anomalous refraction.

The units needed by Airy beam ask for delicate design to realize local loss/gain, considering it is not the point of this work and will not be discussed. Additionally, adaptive

units composed of piezoelectric materials[18, 56] is believed to be capable of realizing such responses, which is advantageous for both passive and active manipulation.

4. CONCLUSION

In this work, we have presented an interface impedance model theoretically and numerically to achieve scattering-free fields. The proposed model is firstly applied to realize perfect anomalous refraction. Then, lossless or lossy form of impedance has been presented to answer the functionalities which are generally obtained through phase modulation. SH plane waves can pass through different-shaped boundaries and generate the desired wave fields without parasitic scattering. After obtaining results consistent with the assumed theoretical field, the design of elastic metasurfaces has been carried out based on lossless zigzag-shaped units. Genetic algorithm is employed to determine the geometric parameters of the units to meet the impedance requirements. The simulated results of the lossless metasurface have shown a great agreement with the theoretical results, confirming further the validity of the proposed interface impedance theory for elastic waves in this work.

The interface impedance model for transmission proposed here can assist in designing elastic metasurfaces with different functionalities and shapes. Except for the SH wave studied, the ideas and methods provided in this work also bring posibilities for wave modes that are more conducive to experimentation, such as in-plane waves and plate waves. We believe that the potentials on precise manipulation based on impedance theory will be demonstrated theoretically and practically with further research.

Acknowledgment

This work has been supported by la Région Grand Est, the Institut CARNOT ICEEL, and the National Natural Science Foundation of China (NNSFC) under Grant Nos. 12122207, 12021002 and 11991032.

References

[1] Nanfang Yu, Patrice Genevet, Mikhail A Kats, Francesco Aieta, Jean-Philippe Tetienne, Federico Capasso, and Zeno Gaburro. Light propagation with phase discontinuities: generalized laws of reflection and refraction. *Science*, 334(6054):333–337, 2011.

[2] Xingjie Ni, Naresh K Emani, Alexander V Kildishev, Alexandra Boltasseva, and Vladimir M Shalaev. Broadband light bending with plasmonic nanoantennas. *Science*, 335(6067):427–427, 2012.

[3] Badreddine Assouar, Bin Liang, Ying Wu, Yong Li, Jian-Chun Cheng, and Yun Jing. Acoustic metasurfaces. *Nature Reviews Materials*, 3(12):460–472, 2018.

[4] Yong Li, Bin Liang, Zhong-ming Gu, Xin-ye Zou, and Jian-chun Cheng. Reflected wavefront manipulation based on ultrathin planar acoustic metasurfaces. *Scientific Reports*, 3(1):1–6, 2013.

[5] Yong Li, Xue Jiang, Rui-qi Li, Bin Liang, Xin-ye Zou, Lei-lei Yin, and Jian-chun Cheng. Experimental realization of full control of reflected waves with subwavelength acoustic metasurfaces. *Physical Review Applied*, 2(6):064002, 2014.

[6] Zhou Hu, Zhibo Wei, Kun Wang, Yan Chen, Rui Zhu, Guoliang Huang, and Gengkai Hu. Engineering zero modes in transformable mechanical metamaterials. *Nature Communications*, 14(1):1266, 2023.

[7] Mingye Zheng, Xiaoning Liu, Yi Chen, Hongchen Miao, Rui Zhu, and Gengkai Hu. Theory and realization of nonresonant anisotropic singly polarized solids carrying only shear waves. *Physical Review Applied*, 12(1):014027, 2019.

[8] Mingye Zheng, Chung Il Park, Xiaoning Liu, Rui Zhu, Gengkai Hu, and Yoon Young Kim. Non-resonant metasurface for broadband elastic wave mode splitting. *Applied Physics Letters*, 116(17), 2020.

[9] Hongfei Zhu, Timothy F Walsh, and Fabio Semperlotti. Total-internal-reflection elastic metasurfaces: Design and application to structural vibration isolation. *Applied Physics Letters*, 113(22):221903, 2018.

[10] Min Soo Kim, Woo Rim Lee, Yoon Young Kim, and Joo Hwan Oh. Transmodal elastic

metasurface for broad angle total mode conversion. *Applied Physics Letters*, 112(24), 2018.

[11] Yabin Jin, Wan Wang, Abdelkrim Khelif, and Bahram Djafari-Rouhani. Elastic metasurfaces for deep and robust subwavelength focusing and imaging. *Physical Review Applied*, 15(2):024005, 2021.

[12] Weikai Xu, Meng Zhang, Zibin Lin, Chenglong Liu, Wuchao Qi, and Wei Wang. Anomalous refraction manipulation of lamb waves using single-groove metasurfaces. *Physica Scripta*, 94(10):105807, 2019.

[13] Hongfei Zhu and Fabio Semperlotti. Anomalous refraction of acoustic guided waves in solids with geometrically tapered metasurfaces. *Physical Review Letters*, 117(3):034302, 2016.

[14] Tian Zhao, Zhichun Yang, Wei Tian, Liyun Cao, and Yanlong Xu. Deep-subwavelength elastic metasurface with force-moment resonators for abnormally reflecting flexural waves. *International Journal of Mechanical Sciences*, 221:107193, 2022.

[15] Youqiang Jiang, Yaolu Liu, Mingquan Kou, Houbo Li, Xiaopeng Wu, Xianjun Zeng, Xiaoyang Bi, Han Zhang, and Ning Hu. Multi-parameter independent manipulation for flexural wave by notched metasurface. *International Journal of Mechanical Sciences*, 214:106928, 2022.

[16] Yizhou Shen, Yanlong Xu, Feng Liu, Fanglong Wang, and Zhichun Yang. 3d-printed meta-slab for focusing flexural waves in broadband. *Extreme Mechanics Letters*, 48:101410, 2021.

[17] Wei Yan and Yuanwen Gao. Steering of flexural wave propagation in tunable magnetorheological elastomers metasurface by modulating magnetic field. *International Journal of Mechanical Sciences*, 237:107793, 2023.

[18] Zoe Yaw, Weijian Zhou, and CW Lim. Anomalous wave control by an adaptive elastic metasurface shunted with negative capacitance circuit. *Journal of Sound and Vibration*, 525:116782, 2022.

[19] Simin Yuan, Ali Chen, and Yuesheng Wang. Switchable multifunctional fish-bone elastic metasurface for transmitted plate wave modulation. *Journal of Sound and Vibration*, 470:115168, 2020.

[20] Xiaoshuang Li, Hongtao Zhou, Yanfeng Wang, and Yuesheng Wang. Modulation of acoustic self-accelerating beams with tunable curved metasurfaces. *Applied Physics Letters*, 118(2):023503, 2021.

[21] Hao Qiu and Faxin Li. Manipulation of shear horizontal guided wave with arbitrary wave fronts by using metasurfaces. *Journal of Physics D: Applied Physics*, 53(28):285301, 2020.

[22] Yongquan Liu, Zixian Liang, Fu Liu, Owen Diba, Alistair Lamb, and Jensen Li. Source illusion devices for flexural lamb waves using elastic metasurfaces. *Physical review letters*, 119(3):034301, 2017.

[23] Shilong Li, Jiawen Xu, and J Tang. Tunable modulation of refracted lamb wave front facilitated by adaptive elastic metasurfaces. *Applied Physics Letters*, 112(2):021903, 2018.

[24] Liyun Cao, Zhichun Yang, Yanlong Xu, and Badreddine Assouar. Deflecting flexural wave with high transmission by using pillared elastic metasurface. *Smart Materials and Structures*, 27(7):075051, 2018.

[25] Yabin Jin, Bernard Bonello, Rayisa P Moiseyenko, Yan Pennec, Olga Boyko, and Bahram Djafari-Rouhani. Pillar-type acoustic metasurface. *Physical Review B*, 96(10):104311, 2017.

[26] Liyun Cao, Zhichun Yang, Yanlong Xu, Shi-Wang Fan, Yifan Zhu, Zhaolin Chen, Brice Vincent, and Badreddine Assouar. Disordered elastic metasurfaces. *Physical Review Applied*, 13(1):014054, 2020.

[27] Hyuk Lee, Jun Kyu Lee, Hong Min Seung, and Yoon Young Kim. Mass-stiffness substructuring of an elastic metasurface for full transmission beam steering. *Journal of the Mechanics and Physics of Solids*, 112:577–593, 2018.

[28] Sung Won Lee, Hong Min Seung, Wonjae Choi, Miso Kim, and Joo Hwan Oh. Broad-angle refractive transmodal elastic metasurface. *Applied Physics Letters*, 117(21):213502, 2020.

[29] Zibin Lin, Weikai Xu, Chengming Xuan, Wuchao Qi, and Wei Wang. Modular elastic metasurfaces with mass oscillators for transmitted flexural wave manipulation. *Journal of Physics D: Applied Physics*, 54(25):255303, 2021.

[30] Jun Zhang, Xiaoshi Su, Yan Pennec, Yun Jing, Xiaofeng Liu, and Ning Hu. Wavefront steering of elastic shear vertical waves in solids via a composite-plate-based metasurface. *Journal of Applied Physics*, 124(16):164505, 2018.

[31] Xiaohui Shen, Chin-Teh Sun, Miles V Barnhart, and Guoliang Huang. Elastic wave manipulation by using a phase-controlling meta-layer. *Journal of Applied Physics*, 123(9):091708, 2018.

[32] Liyun Cao, Zhichun Yang, and Yanlong Xu. Steering elastic sh waves in an anomalous way by metasurface. *Journal of Sound and Vibration*, 418:1–14, 2018.

[33] Yongquan Liu, Zixian Liang, Fu Liu, Owen Diba, Alistair Lamb, and Jensen Li. Source illusion devices for flexural lamb waves using elastic metasurfaces. *Physical Review Letters*,

119(3):034301, 2017.

[34] Guangyuan Su, Yunhao Zhang, Yongquan Liu, and Tiejun Wang. Steering flexural waves by amplitude-shift elastic metasurfaces. *Journal of Applied Mechanics*, 88(5), 2021.

[35] Jun Zhang, Xuebin Zhang, Fulai Xu, Xiangyan Ding, Mingxi Deng, Ning Hu, and Chuanzeng Zhang. Vibration control of flexural waves in thin plates by 3d-printed metasurfaces. *Journal of Sound and Vibration*, 481:115440, 2020.

[36] Xiaoshi Su, Zhaocheng Lu, and Andrew N Norris. Elastic metasurfaces for splitting sv-and p-waves in elastic solids. *Journal of Applied Physics*, 123(9):091701, 2018.

[37] Hao Qiu and Faxin Li. Manipulation of shear horizontal guided wave with arbitrary wave fronts by using metasurfaces. *Journal of Physics D: Applied Physics*, 53(28):285301, 2020.

[38] Yaolu Liu, Houbo Li, Jun Zhang, Xuyang Liu, Liangke Wu, Huiming Ning, and Ning Hu. Design of elastic metasurfaces for controlling shear vertical waves using uniaxial scaling transformation method. *International Journal of Mechanical Sciences*, 169:105335, 2020.

[39] Shin Young Kim, Woorim Lee, Joong Seok Lee, and Yoon Young Kim. Longitudinal wave steering using beam-type elastic metagratings. *Mechanical Systems and Signal Processing*, 156:107688, 2021.

[40] Stéphane Larouche and David R Smith. Reconciliation of generalized refraction with diffraction theory. *Optics letters*, 37(12):2391–2393, 2012.

[41] Yuchi Su, Tungyang Chen, Liheng Ko, and Menghsueh Lu. Design of metasurfaces to enable shear horizontal wave trapping. *Journal of Applied Physics*, 128(17):175107, 2020.

[42] Yongdu Ruan, Xu Liang, and Chuanjie Hu. Retroreflection of flexural wave by using elastic metasurface. *Journal of Applied Physics*, 128(4):045116, 2020.

[43] Liyun Cao, Zhichun Yang, Yanlong Xu, Shiwang Fan, Yifan Zhu, Zhaolin Chen, Yong Li, and Badreddine Assouar. Flexural wave absorption by lossy gradient elastic metasurface. *Journal of the Mechanics and Physics of Solids*, 143:104052, 2020.

[44] Bing Li, Yabin Hu, Jianlin Chen, Guangyuan Su, Yongquan Liu, Meiying Zhao, and Zheng Li. Efficient asymmetric transmission of elastic waves in thin plates with lossless metasurfaces. *Physical Review Applied*, 14(5):054029, 2020.

[45] Guangyuan Su, Zongliang Du, Peng Jiang, and Yongquan Liu. High-efficiency wavefront manipulation in thin plates using elastic metasurfaces beyond the generalized snell's law. *Mechanical Systems and Signal Processing*, 179:109391, 2022.

[46] Ana Díaz-Rubio and Sergei A Tretyakov. Acoustic metasurfaces for scattering-free anomalous reflection and refraction. *Physical Review B*, 96(12):125409, 2017.

[47] Junfei Li, Chen Shen, Ana Díaz-Rubio, Sergei A Tretyakov, and Steven A Cummer. Systematic design and experimental demonstration of bianisotropic metasurfaces for scattering-free manipulation of acoustic wavefronts. *Nature communications*, 9(1):1342, 2018.

[48] Junfei Li, Ailing Song, and Steven A Cummer. Bianisotropic acoustic metasurface for surface-wave-enhanced wavefront transformation. *Physical Review Applied*, 14(4):044012, 2020.

[49] Junfei Li, Ana Díaz-Rubio, Chen Shen, Zhetao Jia, Sergei Tretyakov, and Steven Cummer. Highly efficient generation of angular momentum with cylindrical bianisotropic metasurfaces. *Physical Review Applied*, 11(2):024016, 2019.

[50] Xiuyuan Peng, Junfei Li, Chen Shen, and Steven A Cummer. Efficient scattering-free wavefront transformation with power flow conformal bianisotropic acoustic metasurfaces. *Applied Physics Letters*, 118(6):061902, 2021.

[51] Yongdu Ruan and Xu Liang. Reflective elastic metasurface for flexural wave based on surface impedance model. *International Journal of Mechanical Sciences*, 212:106859, 2021.

[52] José M Carcione. *Wave fields in real media: Wave propagation in anisotropic, anelastic, porous and electromagnetic media*. Elsevier, 2007.

[53] Victor Giurgiutiu. *Structural health monitoring: with piezoelectric wafer active sensors*. Elsevier, 2007.

[54] Li Quan and Andrea Alù. Hyperbolic sound propagation over nonlocal acoustic metasurfaces. *Physical Review Letters*, 123(24):244303, 2019.

[55] Ana Díaz-Rubio, Junfei Li, Chen Shen, Steven A Cummer, and Sergei A Tretyakov. Power flow–conformal metamirrors for engineering wave reflections. *Science advances*, 5(2):eaau7288, 2019.

[56] Shilong Li, Jiawen Xu, and Jiong Tang. Adaptive elastic metasurfaces for wave front manipulation. In *Active and Passive Smart Structures and Integrated Systems XII*, volume 10595, pages 630–635. SPIE, 2018.